Monthly Notices
of the
ROYAL ASTRONOMICAL SOCIETY

MNRAS **497,** 793–808 (2020)
Advance Access publication 2020 July 8

doi:10.1093/mnras/staa1958

Filament intersections and cold dense cores in Orion A North

Chao Zhang,[1] Zhiyuan Ren ,[1★] Jingwen Wu ,[1★] Di Li ,[1,2,3★] Lei Zhu,[4] Qizhou Zhang ,[5] Diego Mardones ,[6] Chen Wang ,[7] Hui Shi,[1] Nannan Yue,[1,2] Gan Luo,[1,2] Jinjin Xie,[1,2] Sihan Jiao,[1,2] Shu Liu,[1,2] Xuefang Xu[1,2] and Shen Wang[1,2]

[1]*National Astronomical Observatories, Chinese Academy of Sciences, A20 Datun Road, Chaoyang District, Beijing 100101, China*
[2]*University of Chinese Academy of Sciences, Beijing 100049, China*
[3]*NAOC-UKZN Computational Astrophysics Centre (NUCAC), University of KwaZulu-parental, Durban 4000, South Africa*
[4]*Chinese Academy of Sciences, South America Center for Astronomy, A20 Datun Road, Chaoyang District, Beijing 100101, China*
[5]*Center for Astrophysics | Harvard and Smithsonian, 60 Garden Street, Cambridge, MA 02318, USA*
[6]*Departamento de Astronomia, Universidad de Chile, Casilla 36-D, Santiago, Chile*
[7]*CSIRO Data61, Sydney, NSW 2015, Australia*

Accepted 2020 June 15. Received 2020 June 6; in original form 2020 January 11

ABSTRACT

We studied the filament structures and cold dense cores in OMC-2,3 region in Orion A North molecular cloud using the high-resolution N_2H^+ (1-0) spectral cube observed with the Atacama Large Millimeter/Submillimeter Array (ALMA). The filament network over a total length of 2 pc is found to contain 170 intersections and 128 candidate dense cores. The dense cores are all displaced from the infrared point sources (possible young stars), and the major fraction of cores (103) are located around the intersections. Towards the intersections, there is also an increasing trend for the total column density $N_{\rm tot}$ as well as the power-law index of the column-density Probability Distribution Function (N-PDF), suggesting that the intersections would in general have more significant gas assembly than the other part of the filament paths. The virial analysis shows that the dense cores mostly have virial mass ratio of $\alpha_{\rm vir} = M_{\rm vir}/M_{\rm gas} < 1.0$, suggesting them to be bounded by the self-gravity. In the mean time, only about 23 per cent of the cores have critical mass ratio of $\alpha_{\rm crit} = M_{\rm crit}/M_{\rm gas} < 1.0$, suggesting them to be unstable against core collapse. Combining these results, it shows that the major fraction of the cold starless and possible pre-stellar cores in OMC-2,3 are being assembled around the intersections, and currently in a gravitationally bound state. But more extensive core-collapse and star formation may still require continuous core mass growth or other perturbations.

Key words: stars: formation – ISM: clouds – ISM: individual objects: Orion A North – ISM: molecules – ISM: structure.

1 INTRODUCTION

Filaments are widely existing structures in molecular clouds and are closely related to star-forming activities (Schneider & Elmegreen 1979; Wang et al. 2008; André et al. 2010; Arzoumanian et al. 2011). Filamentary clouds usually have hierarchical structures (Hacar et al. 2013; Takahashi et al. 2013; Clarke, Whitworth & Hubber 2016; Gómez, Vázquez-Semadeni & Zamora-Avilés 2018) scaled from 0.01 to several parsecs. The theoretical works expect filamentary structures to be responsible for stabilizing the dense-gas and channelling gas into the dense cores or young stellar clusters (Pon, Johnstone & Heitsch 2011; Tan et al. 2014; Smith et al. 2016; Motte, Bontemps & Louvet 2018; Lin et al. 2019), and in some cases more intensely support the mass aggregation via the intersected and merged multiple filaments (e.g. Hill et al. 2011; Myers 2011; Hennemann et al. 2012).

The observational studies have also revealed the universal connection between the filamentary networks and the dense cores and young stars (Arzoumanian et al. 2011; Ragan et al. 2012; Schneider et al. 2012; Henshaw et al. 2016; Kainulainen et al. 2017; Lin et al. 2017; Xu et al. 2018). In some regions, the major filaments in a cloud are connected into a filament-hub system and exhibit possible convergent gas motion towards the hub-area (Hill et al. 2011; Hennemann et al. 2012; Chen et al. 2019a; Treviño-Morales et al. 2019). In other cases, the filaments are resolved into substructures at smaller scales, and the intersected subfilaments are closely associated with multiple or clustered cores or young stellar objects (YSOs) (e.g. Hennemann et al. 2012; Schneider et al. 2012; Henshaw et al. 2016; Lin et al. 2017; Shimajiri et al. 2019), suggesting increased star-forming activities therein.

Despite the spatial association, the physical connection between filaments and dense cores, in particular those at early stages, are still to be further explored. In doing this, one may first need to enlarge the sample of filament structures wherein the individual pre-stellar cores can be resolved to make direct comparison with their parental filaments. Secondly, in addition to the spatial comparison, it further requires a specified study about the key properties of the filaments including their spatial structure, velocity field, and magnetic field, in order to compare their relative importance in the dense core formation. Currently such detailed studies have been performed only

★ E-mail: renzy@nao.cas.cn (ZR); jingwen@nao.cas.cn (JW); dili@nao.cas.cn (DL)

in a limited number of regions (e.g. Liu et al. 2018; Wang et al. 2019).

Orion A cloud is one of the most favourite sites to study the cold dense filaments and cores (Johnstone & Bally 1999; Nutter & Ward-Thompson 2007; Sadavoy et al. 2010; Shimajiri et al. 2015; Kirk et al. 2017; Hacar et al. 2018). Its main body is an Integral-Shaped dense Filamentary cloud (denoted as ISF) elongated over the Orion Nebular Cluster (ONC) from North to South. The cloud should have a distance comparable to the ONC that is $D = 388 \pm 5$ pc (Kounkel et al. 2017). In recent work, using the ALMA+IRAM 30 m combined data of N_2H^+ $J = (1 - 0)$ transition and the HiFIVE algorithm, Hacar et al. (2018, H18 hereafter) analysed the dense gas in Orion A, revealed the peculiar fine structure of intertwined fibres within major filaments, and discussed their evolutionary state regulated by the gas density. A series of relevant works were also addressed to study the dense clumps and YSOs therein (Salji et al. 2015; Shimajiri et al. 2015; Da Rio et al. 2016; Kirk et al. 2017). With general physical conditions and YSO catalogue well documented, it is desirable to further study the internal filament structures around the individual dense cores, thereby contributing an updated sample to demonstrate their mutual evolution.

In this work, we present an observational study of the filaments in Orion A North (OMC-2,3) using the high-resolution N_2H^+ $J =$ (1-0) transition observed with the Atacama Large Millimeter/submillimeter Array (ALMA). The N_2H^+ (1-0) line has a high critical density of 1.5×10^5 cm^{-2} and a low degree of depletion in cold dense gas due to its low tendency of adhering to particles (Bergin & Langer 1997; Caselli et al. 2002; Pagani, Daniel & Dubernet 2009; Miettinen 2014). It is thus continuously adopted (following H18) in this work to study the gas structures around the individual cores within the ISF. With high angular resolution reaching 1000 AU scale, the parental cores of individual YSOs can be resolved (e.g. Ren, Li & Chapman 2014; Kainulainen et al. 2017; Matsushita et al. 2019). Orion A cloud contains a large fraction of dense gas still in a cold and quiescent state (Salji et al. 2015; Kainulainen et al. 2017; Hacar et al. 2018), thus provides an ideal sample to study the initial evolutionary state of the dense cores. In addition, extensive infrared surveys are carried out to identify the YSOs and clusters in this cloud (Megeath et al. 2012; Salji et al. 2015; Shimajiri et al. 2015), so that the evolutionary states of the molecular cores, in particular the pre- and protostellar ones, can be classified from their spatial association with the catalogued YSOs.

In this work we used several different methods to quantify the gas assembly in the filaments. First, the dynamical models suggested that the column-density probability distribution function (N-PDF) can estimate the turbulence decay and density increase due to the self-gravity (Krumholz, McKee & Klein 2005; Hennebelle & Chabrier 2011; Padoan & Nordlund 2011). The N-PDF properties, including its column density range, power-law tail, and the spatial variation, can give a quantitative estimate for the dense-gas assembly and star-forming efficiency (e.g. Federrath & Klessen 2013; Chen et al. 2018). Secondly, we calculated the virial and critical masses of the cores Li et al. (2013), which can measure their gravitational binding state and tendency to collapse, respectively.

The following contents of this paper are organized as follows: In Section 2, we introduce the observations and data reduction, and describe the algorithm used to extract the filament structures from the line emission data cube. In Section 3, we describe the measurement of the gas distribution along the filaments and around the intersections, and the estimation of the core stabilities. The evolutionary stage and the trend of star formation of these gas components are discussed in Section 4. The major findings are summarized in Section 5.

Table 1. Field centre coordinates for the mosaic mapping.

No.	RA (hh:mm:ss)	Dec (dd:mm:ss)	On-source time[a] (12 m, 7 m) (min)
(OMC-3)			
01	05:35:14.51	−04:59:32.8	17.48, 13.96
02	05:35:16.44	−05:00:06.4	17.48, 13.96
03	05:35:18.26	−05:00:33.6	17.48, 13.96
04	05:35:20.25	−05:00:59.2	17.48, 13.96
05	05:35:22.11	−05:01:28.0	17.48, 13.96
06	05:35:23.73	−05:01:57.6	17.48, 13.96
07	05:35:25.44	−05:02:30.4	17.48, 13.96
08	05:35:26.02	−05:03:10.4	17.48, 13.96
09	05:35:26.35	−05:03:51.2	17.48, 13.96
10	05:35:26.30	−05:05:29.6	17.48, 13.96
11	05:35:26.83	−05:04:44.0	17.48, 13.96
(OMC-2)			
12	05:35:23.51	−05:07:24.8	17.48, 13.96
13	05:35:24.64	−05:08:07.2	17.48, 13.96
14	05:35:25.07	−05:08:54.4	17.48, 13.96
15	05:35:26.30	−05:09:49.6	17.48, 13.96
16	05:35:26.67	−05:10:36.0	17.48, 13.96
17	05:35:25.12	−05:12:16.0	17.48, 13.96
18	05:35:22.33	−05:12:36.8	17.48, 13.96
19	05:35:20.83	−05:13:11.2	17.48, 13.96
20	05:35:21.37	−05:14:20.8	17.48, 13.96
21	05:35:20.46	−05:14:57.6	17.48, 13.96
22	05:35:19.12	−05:15:31.2	17.48, 13.96
23	05:35:18.42	−05:13:03.2	17.48, 13.96
24	05:35:22.44	−05:10:12.0	17.48, 13.96
25	05:35:25.81	−05:11:26.4	17.48, 13.96

Note. [a]The On-source integration time for each pointing (see Fig. 1 for the mapping areas of the pointings). The two values correspond to 12 and 7 m (ACA) arrays, respectively.

2 DATA REDUCTION AND PROCESSING

2.1 Data and observation

The ALMA observation of the N_2H^+ (1-0) transition in OMC-2,3 (proposal ID 2013.1.00662.S, PI: Diego Mardones) was carried out during 2014 November and 2015 August in Band 3. Four bands were used, one of which covered the N_2H^+ (1-0) transition at $f =$ 93.173 GHz with a channel width of $\Delta V_{\rm chan} = 0.1$ km s^{-1}. We used the 12 m main array and the 7 m Atacama Compact Array (ACA) to perform a mosaic mapping. There are 14 pointings towards the OMC-2 and 11 pointings towards OMC-3. The pointing centres and on-source integration time are presented in Table 1. In observation, the 12 m array is at the nearly most compact configuration, with the shortest baseline of 5.2 $k\lambda$, corresponding to a spatial coverage up to 29 arcsec. The 7 m array (ACA) has a fixed configuration with spatial coverage of 13–73 arcsec. The entire data cube thus has a continuous coverage from 3 to 73 arcsec, which is sufficient to detect the filament structures in individual gas clumps, which have diameters of $2r \leq$ 0.1 pc (Kirk et al. 2017).

For the 12 m array data, we used J0423−0120, J0501−0159, and J0750+1231 as bandpass calibrators, J0517−0520 as phase calibrators, and J0423−013 as the flux calibrator. For the ACA data,

we adopted J0501−0159 and J0607−0834 as the bandpass calibrator, J0541−0541 and J0607−0834 as phase calibrators, and Callisto and J0423−0120 as flux calibrators. The observational data were manually calibrated for each EB with CASA 4.4.0. We combined the UV data sets of the 12 m array and ACA and CLEANed it in CASA using the interactive model. The restored image was corrected for the primary-beam response. The synthesized full-width half-maximum (FWHM) beam size is 3 arcsec × 3 arcsec. The rms level of the final maps is 7 mJy beam^{-1} at a spectral resolution of 0.1 km s^{-1}, corresponding to $T_b = 0.11$ K.

2.2 Extracting the filamentary structures in PPV space

In previous studies, various algorithms have been applied to analyse the gas structures in molecular clouds, including Curvelet Transform (Starck, Donoho & Candès 2003), Filfinder (Koch & Rosolowsky 2016), and HiFIVE (Hacar et al. 2013). Curvelet Transform can enhance the input elementary structure, especially the elongated features in the data, but it cannot extract filaments in spectral data cube in the Position–Position–Velocity (PPV) space. Filfinder is capable of uniformly extracting the hierarchical filament structures. It can have stable performance even if the image has large intensity variation, but like the curvelet Transform, it also deals with 2D images. HiFIVE is developed to process the 3D data cube. As shown in H18, it is powerful in resolving the gas structures in PPV space. It can identify each velocity-coherent gas structure in the PPV space, and will clearly divide the different structures. These structures can be further modelled using 1D paths, such as filaments and fibres.

Another algorithm for processing 3D data cube is the Discrete Persistent Structures Extractor (DisPerSE; Sousbie 2011). This algorithm can sensitively identify the elongated gas structures in any 3D data cube above the adopted intensity threshold. It has been commonly used in cosmic data set to identify the filaments and voids. DisPerSE requires a filament to go through one or more saddle points. At a saddle point, there are two particular directions along which the intensity profiles rightly have local maximum and local minimum at this point, respectively. For a saddle point in the filament, the two directions are usually along and perpendicular to the filament, respectively. DisPerSE requires each filament path to contain at least one saddle point. An isolated and elongated single dense core has no internal saddle point thus would not be misidentified as a filament. The extracted filament structures are stable against the intensity variation below the intensity threshold.

Both HiFIVE and DisPerSE can model the gas structures in PPV data cube. Since HiFIVE has been already applied to Orion A in H18, we adopted DisPerSE in this work. DisPerSE would first extract the individual filament paths above the threshold and allow us to inspect their intersections at the next step. Following the previous studies (e.g. Arzoumanian et al. 2011; Sousbie 2011; Schneider et al. 2012), we adopted the 5σ level as the threshold. In our data cube, it corresponds to $5\sigma = 35$ mJy beam^{-1} in the current data set.

After the filament extraction, we examined the possible misidentifications. The misidentified filament paths would go through (i) separated cores or (ii) 2D sheet-like structures. We found that the entire filament structure is located in the emission region above the 5σ limit, while the isolated cores are not covered by the filaments. Meanwhile, the filament paths are measured to have full widths in a narrow range of $w_{\rm fil,\,full} = 14 \pm 4$ arcsec above 5σ (or FWHM widths of $w_{\rm fil,\,FWHM} = 7 \pm 2$ arcsec) and line widths of $\Delta V = 0.5 \pm 0.2$ km s^{-1}, suggesting that the paths should trace the dense gas elongation in one dimension, while the sheet-like morphologies are rare.

3 RESULT

3.1 Filaments and intersections: overall properties

The integrated N_2H^+ (1-0) emission and the filament paths extracted by DisPerSE are displayed in five sub-areas. Each sub-area contains a frame of relatively discrete gas structure. Fig. 1(a) shows the entire emission region in OMC-2,3 overlaid on the *Spitzer*/IRAC 8 μm continuum emission. Fig. 1(b) shows the 3D structure of the filament paths in Area-1. In Fig. 1(c), the filament paths are plotted together with the N_2H^+ emission in the PPV data cube, wherein the hyperfine component of N_2H^+ ($1_0 - 0_1$) is adopted to plot and analyse the gas structures in the PPV space. This component is isolated from the other HFCs (see Fig. 5) and would most clearly demonstrate the velocity distribution of the cold dense gas.

The N_2H^+ (1-0) emission in the sub-areas are shown in Fig. 2. The filament paths projected on the plane of the sky are displayed in yellow lines. The intersections and local emission peaks are labelled with circles and plus symbols, respectively. Based on the observed gas distributions and intensity variation over the filaments, we posed a few criteria in selecting and denominating the typical gas structures:

(1) an *intersection* represents a position where three or more filament paths are connected;

(2) a *filament path* represents a segment between two adjacent endpoints. An endpoint could be either an intersection or an isolated terminal;

(3) a *branch* represents a single filament path between an intersection and a terminal;

(4) a *local emission peak* should exceed the surrounding emission intensity above 5σ intensity (35 mJy beam^{-1} or 0.35×10^{23} cm^{-2}). The surrounding level is adopted as the average emission intensity at $r = 7$ arcsec, satisfying $2r = \overline{w}_{\rm fil,full} = 14$ arcsec. This is based on the consideration that the dense gas assembly usually has comparable or smaller spatial extents than the filament width.

(5) a *candidate core* is selected from the local emission peaks if it is dominated by a single velocity component in its N_2H^+ spectrum. The single velocity component guarantees that the emission peak is more likely tracing a real mass assembly instead of overlapped filaments. The exclusion of overlapped filaments are described in detail in Section 3.2.

As shown in Fig. 2, in general, the output filament paths are closely associated with the observed emission features. Their relation can be described in three major aspects: (i) the identified filament paths go through all the emission features above the 5σ detection limit; (ii) the spatial distribution of the filament paths are coherent with the spatial extents of the emission features; (iii) the major fraction of the emission regions have intersected filaments with relatively short filament paths ($l < 20$ arcsec). In contrast, a few very elongated structures ($l \geq 20$ arcsec) are identified as long filament paths, as labelled in Fig. 2.

As shown in Fig. 2, the filament intersections are widely distributed over the observed region. Each intersection often have three or four filament paths, including one branch and other two or more paths that are connected to other intersections. In some cases, the paths from one intersection are all connected to other intersections. As a result, these filament paths could become encircled, forming a ring-like morphology. A typical ring in Area-3 is labelled with the dashed box

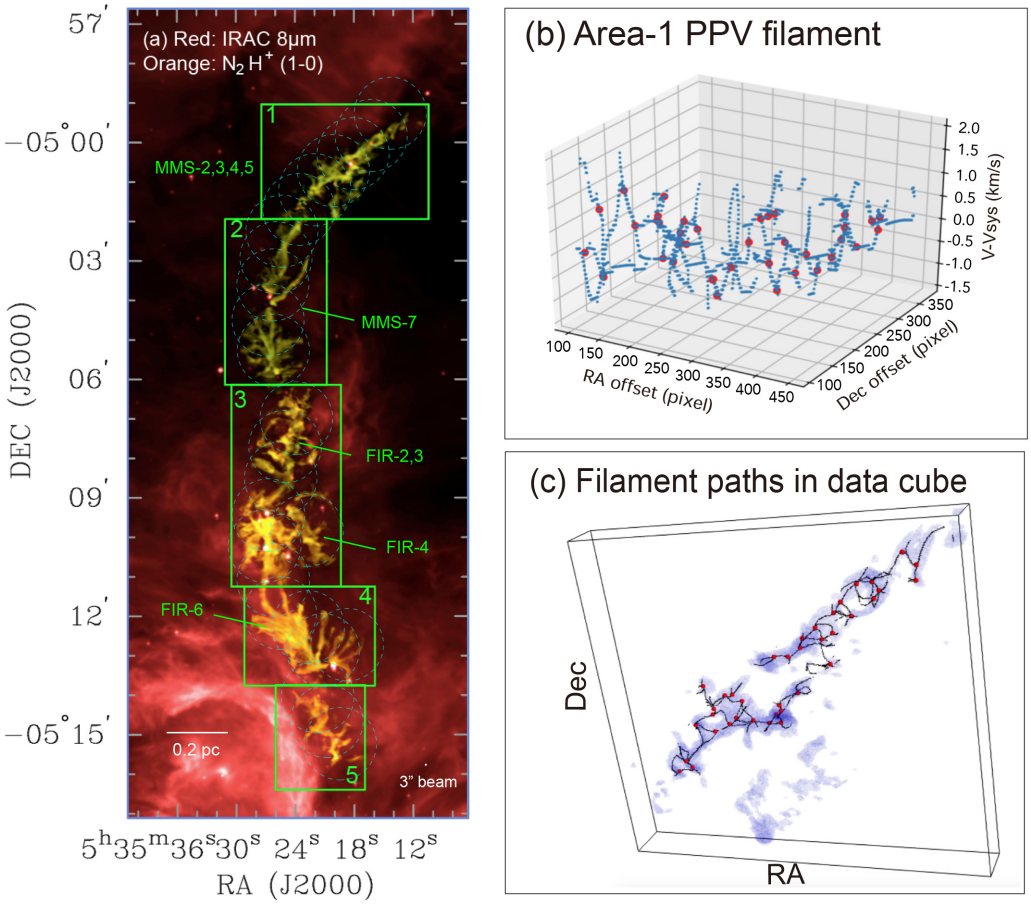

Figure 1. (a) The integrated ALMA N_2H^+ ($1_0 - 0_1$) image (yellow region) overlaid on the *Spitzer*/IRAC 8 μm image (red image) (Megeath et al. 2012). The N_2H^+ image only exhibits the central integral-shaped filament (ISF). The five sub-areas are labelled with boxes. Each area contains relatively condensed filament structures that are reasonably separated from the adjacent areas. Area-1,2,3 belong to OMC-3 and Area-4,5 belong to OMC-2. The dashed circles indicate the field of view (primary beam) of each pointing centre for the mosaic mapping. (b) An example of the filament paths modelled by DisPerSE in Area-1 in PPV space. The blue dashed lines represent the filament paths and the red dots are the intersections. (c) The filament paths overlaid with the emission regions in the data cube. The blue-coloured body represents the line emission in the data cube above the 5 σ detection limit.

in Fig. 2. A series of more complicated multiple rings can be seen in Area-1, in particular MMS-2,3 region. This region was revealed to have complicated hierarchical structure of dense cores aligned over the filament (Takahashi et al. 2013). The fragmentation and dense core formation could be influenced by the closely intersected filament rings.

The filament structures are compared with fibres identified by H18, as shown in Fig. 3. The left-hand panel shows the fibres in H18, which extend over OMC-1,2 and a part of OMC-3. The right-hand panel shows the fibres overlaid in OMC-2 FIR-2,3,4 region, which is covered in both H18 and this work. As the figure shows, for each fibre that has overlap with the N_2H^+ filaments, its direction is in parallel with the bulk gas elongation of the filament paths. But the individual filament paths are mostly shorter than the fibres, and the exact overlap between the fibres and filament paths is rare. This is within our expectation since the fibres would tend to trace large-scale structures because of two reasons. First, the N_2H^+ image in H18 also include a component from the single-dish data (IRAM 30 m), which mostly trace the spatial scales above 30 arcsec (IRAM 30 m beam size). Secondly, the fibre morphology also depends on HiFIVE algorithm. HiFIVE would first cover the entire area of each velocity-coherent structure, then extract the principal axis of the structure as the fibre direction. In this process, the fibre would mainly delineate the overall extension of the structure, and be less sensitive to the internal variations (scale <30 arcsec).

3.2 Intersections: velocity distribution

We examined the gas distribution and kinematical features around the intersections based on their velocity distributions. First, some partly overlapped filaments could be actually separated along the line of sight, the overlapped areas are thus not real intersections. We can eliminate such 'pseudo-intersections' based on the velocity distribution. One can assume each filament to have a distinct velocity, so that if two filaments are separated in the PPV space, they are also likely separated along the line of sight. This assumption is adopted by other works to identify the intertwined filaments or fibres (e.g. Hacar et al. 2013; Shimajiri et al. 2019).

The second scenario to be cautioned is the mass transfer flow along the filament. The gas flow can also generate large velocity variation near the intersections (e.g. Peretto et al. 2014). But the transfer flow is characterized by a sudden velocity change and around the centre, which indicates the gas flow being accelerated and halted at the central YSO. In contrast, the overlapped velocity components would have more separated velocities and less steep velocity gradient, so

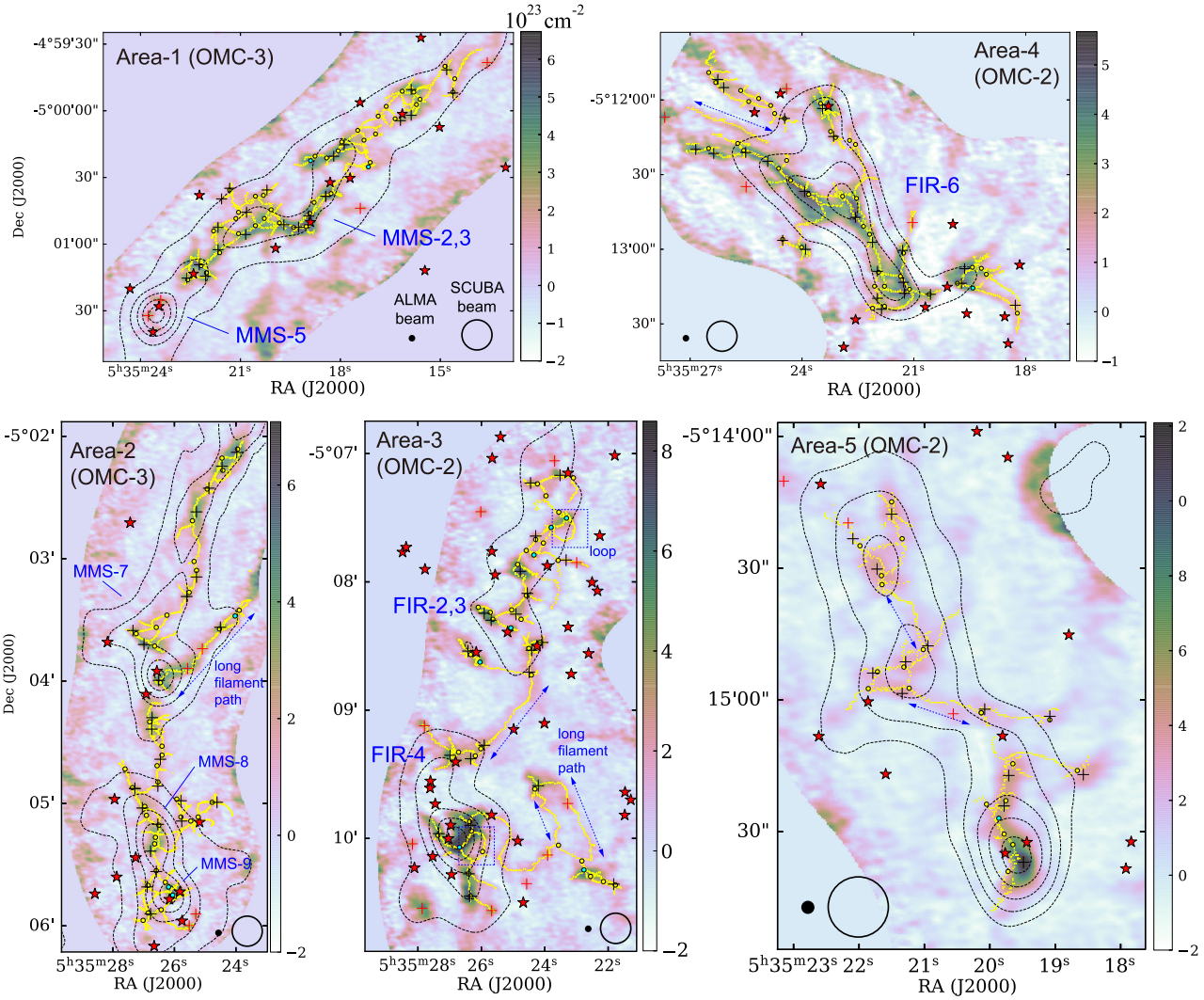

Figure 2. The N_2H^+ emission in each sub-area (false-colour image). The intensity is converted to the total gas column density in unit of 10^{23} cm^{-2} using equation (1). The overlaid dashed contours represent the JCMT/SCUBA 850 μm continuum map (Johnstone & Bally 1999). The contour levels are 10, 30, 50, 70, 90 per cent of the local maximum. Also overlaid on the figure are the DisPerSE-modelled filament paths (yellow dotted lines) projected on to the RA-Dec plane, real, and pseudo intersections (yellow and cyan dots, respectively), local emission peaks (plus), and YSOs (stars) identified from infrared point sources (Megeath et al. 2012). Among the local emission peaks, the black ones denote those near the intersections within a distance of 7 arcsec ($\overline{w}_{\rm fil,FWHM}$), while the red ones denote those more distant from the intersections, e.g. those on the long filament paths or displaced from the ISF. The representative long paths and a typical encircled structure (loop) are labelled with blue dashed arrows and boxes, respectively. In each sub-area, the gas clumps and young stellar clusters are labelled with the blue characters following the denotation in Li et al. (2013) and references therein.

that each velocity component would extend smoothly along the PV-cut direction, instead of having a drastic variation over the centre.

The three typical cases, including an intersection with single velocity component, a pseudo intersection, and an intersection with large velocity gradient, are shown in three columns in Fig. 4. In each column, the upper panel shows the filament paths overlaid on the integrated N_2H^+ emission, the middle and lower panels show the position–velocity (PV) diagrams along the possible gas elongation (major axis) and the transverse direction (minor axis) as denoted in the upper panel.

In the example of one single velocity component (left-hand column), the three filaments have a consistent systemic velocity of $V_{\rm sys} = 11.4\,{\rm km\,s^{-1}}$ at the intersection (upper panel). The PV diagrams (middle and bottom panels) show that the bulk of line emission is confined within a velocity range of $V - V_{\rm sys} = \pm 0.3\,{\rm km\,s^{-1}}$, which is comparable to the average line width of $\overline{\Delta V} = 0.5\,{\rm km\,s^{-1}}$ of the N_2H^+ emission region, as labelled with red dashed lines.

Around the pseudo intersection (middle column), the overlapped filaments with different velocities can be discerned from their paths (upper panel), and the components at different velocities ($V - V_{\rm sys} = 0$ and $0.6\,{\rm km\,s^{-1}}$) have comparable intensities at the central position (offset = 0) as labelled with dashed lines in the PV diagrams.

For the intersection with large velocity gradient (right-hand column), the PV diagrams also exhibit much broader velocity distribution than $\overline{\Delta V}$, but the multiple velocity components are not overlapped at the centre. Instead, they become converged into a relatively narrow range that is also comparable to $\overline{\Delta V}$.

The comparison among the three cases suggests that one can use $\overline{\Delta V}$ as a threshold to distinguish the simple velocity component from more complicated cases. If an intersection has velocity variation

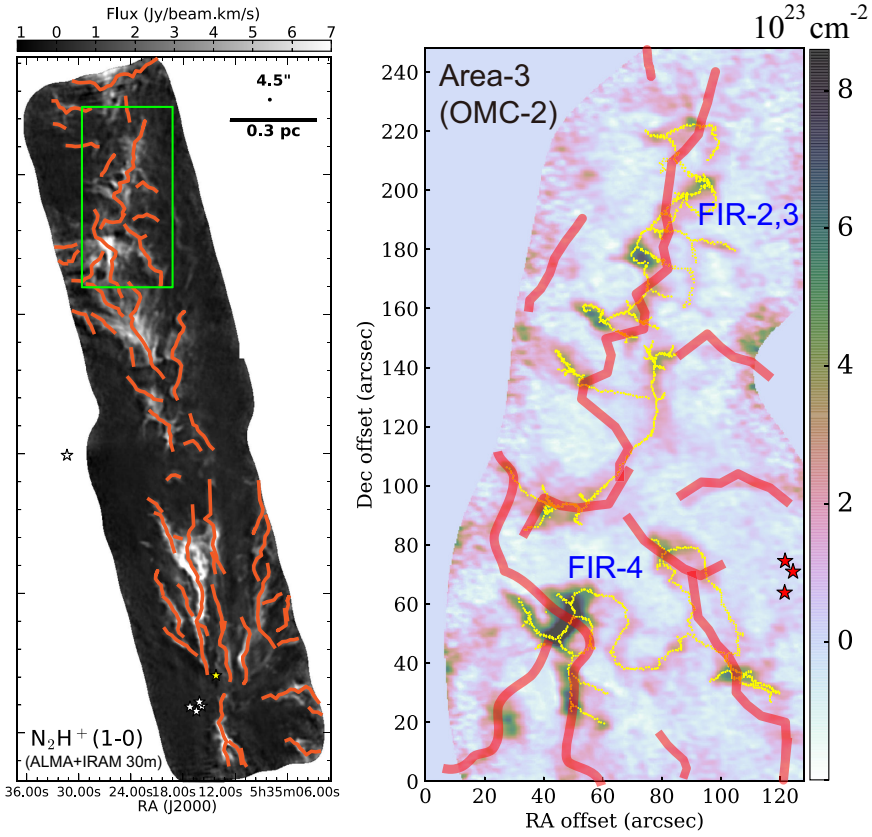

Figure 3. Left-hand panel: The principal axes of the fibres identified by the HiFIVE analysis over OMC-1,2,3 regions (Hacar et al. 2018, Figure 4 therein). Right-hand panel: The fibres (thick red segments) overlaid on the current N_2H^+ emission and the filament structures extracted by DisPerSE, same as that shown in Fig. 2.

significantly exceeding $\overline{\Delta V}$ in its surroundings, it would be suspected to have multiple components. According to this criterion, we selected 156 intersections with simple velocity distributions ($\Delta V \leq \overline{\Delta V}$) and 34 intersections that have large velocity variations. Among these intersections, 14 ones are found to be possible pseudo intersections. The other 20 ones may have largely velocity gradients instead of multiple components. So altogether we have 176 intersections that are considered to be real.

We note that the selection based on ΔV would still be insufficient to exclude all the overlapped filaments. The exceptional ones would represent overlapped filaments with nearly equal $V_{\rm sys}$ so their line profiles are not evidently distinguished. We suppose this scenario to be scarce because the different filaments usually have noticeably different velocities (>0.3 km s^{-1}). If an intersection has a single-peaked spectrum and have relatively narrow line width ($\Delta V < \overline{\Delta V}$), its parental filaments are more likely to be indeed merged in space, while a pseudo-intersection would tend to have multiple spectral components.

3.3 Dense cores: column density, mass, and spatial distribution

As described in Section 1, a key property to explore is the gas assembly and dense core formation in the filaments. We inspected the N_2H^+ emission at the local emission peaks (candidate dense cores). We also examined the spectra at the emission peaks to exclude those with evident multiple velocity components. The excluded ones are mostly around the pseudo-intersections.

Over the ISF, we altogether identified 128 candidate cores that have single spectral component and exceed the 5 σ detection limit. Their locations are labelled with plus symbols in Fig. 2. We compared their spatial distributions with the filament intersections. As a result, 119 intersections (70 per cent) are found to have nearby cores within a distance of 5 arcsec. Inversely, among the dense cores, 103 (79 per cent) are located close to the intersections. The other 25 cores are located on the long filament paths or displaced from the filaments. These cores are labelled with red crosses in Fig. 2. It is noteworthy that the intersections and the nearby cores usually have an offset of 3 to 5 arcsec and are only occasionally fully overlapped. This indicates that the filament extraction by DisPerSE is not biased to the dense cores.

To examine the physical properties of the cores, we first derived the total column density $N_{\rm tot} = N({\rm H_2 + H\,I})$ from the N_2H^+ emission following the normal procedure (e.g. Caselli et al. 2002; Henshaw et al. 2014):

$$N_{\rm tot} = \frac{I_{\rm tot}}{X({\rm N_2H^+})} \frac{8\pi}{\lambda^3 A_{\rm ul}} \frac{g_l}{g_u} \times \frac{1}{J(T_{\rm ex}) - J(T_{\rm bg})} \times \frac{1}{1 - \exp(-h\nu/k_{\rm B}T_{\rm ex})} \times \frac{Q_{\rm rot}(T_{\rm ex})}{g_l \exp(-El/k_{\rm B}T_{\rm ex})}, \quad (1)$$

wherein $I_{\rm tot}$ is integrated intensity of the N_2H^+ (1-0) line, $X(N_2H^+)$ is the N_2H^+ abundance, $A_{\rm ul} = 3.63 \times 10^{-5}$ s^{-1} is Einstein coefficient (Schöier et al. 2005), g_u and g_l are the statistical weights of the upper and lower states, respectively; $J_\nu(T_{\rm ex})$ and $J(T_{\rm bg})$ are equivalent Rayleigh-Jeans excitation and background temperatures, respectively; $Q_{\rm rot}(T_{\rm ex})$ is the partition function at the excitation

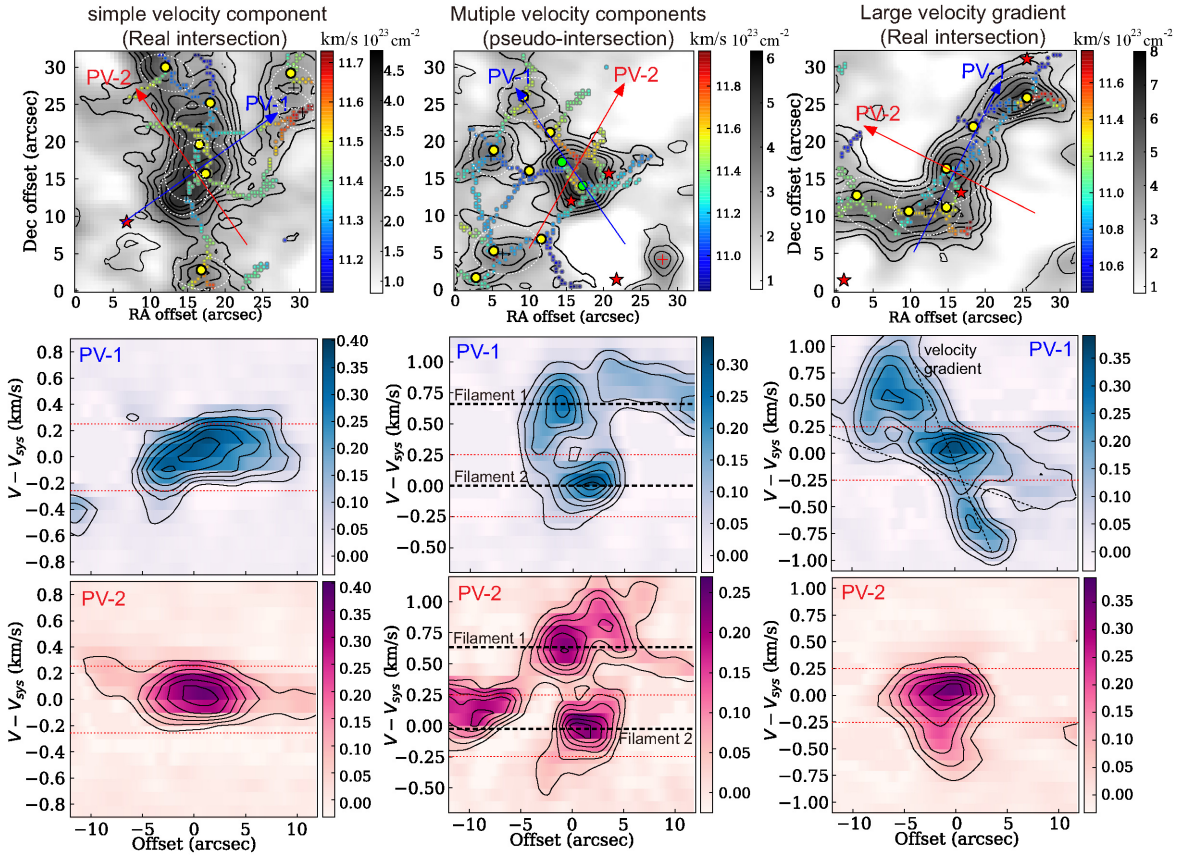

Figure 4. The gas distributions and position–velocity diagrams over three representative gas structures, (i) real intersection with simple velocity component (in MMS-8,9), (ii) likely pseudo-intersection (in MMS-8,9), and (iii) real intersection with evident velocity gradient (in MMS-2,3). They are shown in the three columns, respectively. In each column, upper panel is the integrated N_2H^+ ($1_0 - 0_1$) image (grey scale and contours). The grey scale starts from 0.8×10^{23} cm^{-2}, which is the average level of the diffuse emission away from the ISF. The contour levels are 15, 30, 45, 60, 75, 90 per cent of the local maximum. The coloured dots represent the filament structures modelled by DisPerSE, with the colour scale indicating the radial velocity. The yellow and green circles represent real and pseudo intersections, respectively. The crosses are the local emission peaks above $5\,\sigma$ level. The red stars are the YSOs from the catalogue (Megeath et al. 2012). The directions to plot the P–V diagrams are denoted with red and blue arrows. The two directions are along the major and minor axes of the central core. Middle and lower panels are the P–V diagrams along the major and minor directions, respectively. The velocity components and velocity gradients are denoted with black dashed lines. The red dotted lines represent the velocity range of ± 0.25 km s^{-1} corresponding to the average line width of 0.5 km s^{-1}.

temperature T_{ex}. The intensity I_{tot} can be derived from the optically thin component $JF_1 = (1_0 - 0_1)$ using $I_{tot} = 1/R_i \int T_b dv$, where $R_i = 0.11$ is its relative statistical weight.

For the N_2H^+ abundance, we also referred to the latest measurement in H18 that is $X(N_2H^+) = (7.5 \pm 7) \times 10^{-10}$. The spatial variation of $X(N_2H^+)$ should be mainly caused by stellar heating. This effect can be evidently seen in two typical regions, OMC-3 MMS-5 and OMC-2 FIR-4 (Fig. 2), wherein N_2H^+ emission becomes largely devoid around the YSOs. Except these areas, the N_2H^+ emission is very coherent with the SCUBA 850 μm emission, suggesting that $X(N_2H^+)$ should have a uniform distribution. Since this work is mainly focused on the cold dense gas component, it should be reasonable to assume a relatively stable level of $X(N_2H^+)$.

The excitation temperature T_{ex} can be estimated from fitting the hyper-fine structure of the N_2H^+ spectra. We performed spectral fitting using the Python package PYSPECKIT (Ginsburg & Mirocha 2011), which can generate a theoretical spectrum using the radiative transfer functions. The free parameters include T_{ex}, optical depth τ, systemic velocity V_{sys}, and the velocity dispersion $\sigma_v = \Delta V / \sqrt{8 \ln 2}$. An example of spectral fitting is shown in Fig. 5(a). One can see that the observed spectrum can be closely reproduced by adjusting the model parameters. Over the N_2H^+ emission region, the temperature is measured to be $T_{ex} = 15 \pm 4$ K (Fig. 5b). It can be compared with the kinetic temperature T_{kin} measured from the NH_3 lines (Li et al. 2013; Kirk et al. 2015). These two works provided similar values of $T_{kin} = 16$ to 27 K in Orion A. Their lower limit is close to the current value of $\overline{T}_{ex}(N_2H^+) = 15$ K. Since the N_2H^+ should usually trace cooler and denser gas components than NH_3 (Shirley 2015; Chen et al. 2019b), it should be reasonable to adopt a constant $T_{ex} = 15$ K in calculation. It is also comparable to the average gas temperature of 15 K in infrared dark clouds (Chira et al. 2013). The N_2H^+ ranges of the filaments and cores are presented in Table 2.

We measured the spatial extent of each core from its N_{tot} profile over the emission peak. The N_{tot} distributions along the major and minor axes of each core are overlaid in Fig. 6 (upper panels). Along the minor axis, the N_{tot} profiles rapidly decrease towards the outer part (offset $= \pm 7$ arcsec) and reaches the surrounding level of $\overline{N}_{tot} = 0.7 \times 10^{23}$ cm^{-2}. Along the major axis, the N_{tot} profiles are much more flattened, decreasing to the level of $\overline{N}_{tot} = 1.5 \times 10^{23}$ cm^{-2} at offset $= \pm 12$ arcsec. The spatial extent of a core can be characterized by its major and minor axes. The cores are measured to have diameters of $2r_{maj} = 8.5 \pm 3.0$ arcsec (3300 ± 1100 AU) and $2r_{min} = 7.5 \pm 3.0$ arcsec (2910 ± 1100 AU), which are comparable to the filament width $\overline{w}_{fil,FWHM} = 7$ arcsec. The major and minor axes

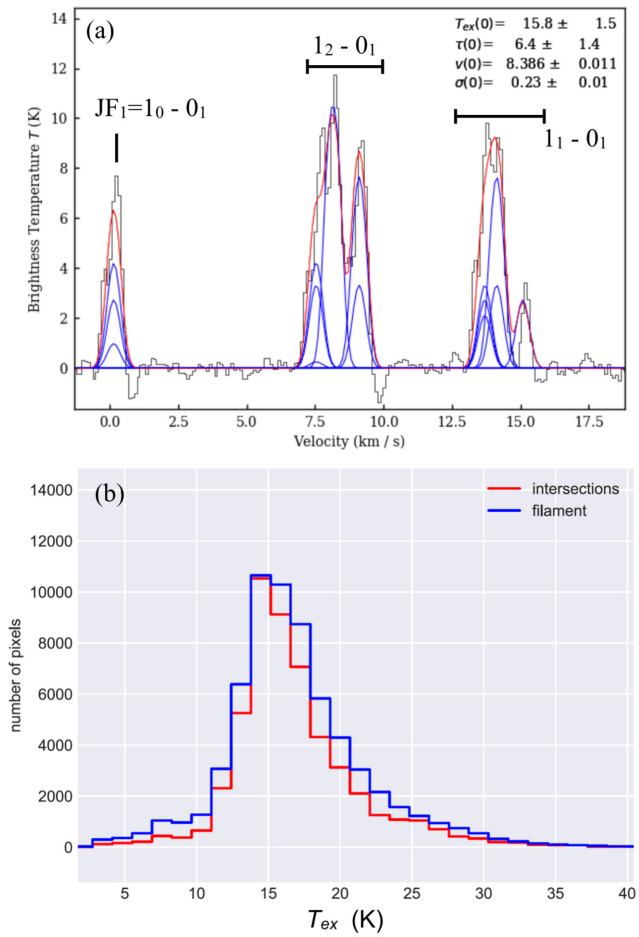

Figure 5. (a) An example spectrum from OMC-2 FIR-6 and the hyper-fine fitting. The black line is the observed spectrum. The red line is the optimized model spectrum, with the individual HFCs shown in blue lines. Each HFC is a transition between JF_1F levels. The blue lines represent all the JF_1F transitions, and their frequencies are adopted from Pagani et al. (2009). The three major groups of JF_1 transitions are labelled on the spectrum. We note that the $JF_1 = 1_0 - 0_1$ group contains three F transitions with the same frequencies. The physical parameters of the best-fitting spectrum are labelled on the panel. (b) The histogram of T_{ex} distribution over the ISF. The areas around intersections and the filament paths are separately sampled. Their distributions are presented in red and blue histograms, respectively.

are nearly parallel with and perpendicular to the local filament path, respectively (see Fig. 4). The morphologies of the cores agree with the expectation that they are being formed within the filaments.

We calculated the core mass from its integrated flux using $M_{\rm core} = \mu m_{\rm H} \int N_{\rm tot} {\rm d}A$, wherein $m_{\rm H}$ is the molecular hydrogen mass and $\mu = 2.33$ is the mean molecular weight (Myers 1983). The mass of the filament paths are also estimated from the flux within the average full width of the filament paths ($\overline{w}_{\rm fil,full} = 14$ arcsec). The derived mass scales are presented in Table 2. We note that in calculating the core mass, the surrounding levels of $N_{\rm tot}$ (solid horizontal lines in Figs 6a and b) are not subtracted. This is based on the consideration that the mass assembly in the cores is taking place on the basis of the surrounding gas density, thus should exclude the contribution of the surrounding level. Although the surrounding level could also include the diffuse gas in the back- and foreground, this component would be insignificant because the average $N_{\rm tot}$ away from ISF is very low (see Fig. 7a and Section 4.1).

Over the entire N_2H^+ emission region, the long filament paths have much lower $N_{\rm tot}$ variation along their paths compared to the intersected ones. For example, Area-3 (Fig. 2, lower middle panel) contains three typical long paths. They have $N_{\rm tot} \leq 2 \times 10^{23}$ cm^{-2} over the total length of ∼40 arcsec. The $N_{\rm tot}$ values significantly increases only towards the ending points, where the paths are already intersected with other filaments. There are only a few cores located on the long filament paths, such as the one in Area-2 (OMC-3 MMS-7, labelled with a blue arrow). There are two candidate cores on this path, but the overall $N_{\rm tot}$ distribution still further increases towards the two ending points, which are both intersections.

3.4 Dense cores: velocity dispersion

With a channel width of $\Delta V_{\rm chan} = 0.1$ kms^{-1}, the N_2H^+ line profile can be resolved at a favourable accuracy, enabling us to measure the velocity dispersion of each core thereby estimate the internal pressure support against the self-gravity.

The N_2H^+ (1-0) velocity dispersion is measured together with $T_{\rm ex}$ from the spectral fitting. Figs 6(c) and (d) exhibit the $\sigma_v(r)$ profiles along the major and minor axes of each local peak, respectively. Unlike the $N_{\rm tot}(r)$ profiles, $\sigma_v(r)$ profiles do not exhibit any evident increase towards the core centres. Instead, they are mostly confined in the range of $\sigma_v = (0.05, 0.25)$ km s^{-1} over offset of (−10 arcsec, 10 arcsec). The average $\sigma_v(r)$ profiles even exhibit a slight decrease from $\sigma_v = 0.13$ to 0.10 km s^{-1} towards the centre along both the major and minor axes. This result suggests that the candidate dense cores tend to have comparable or even smaller velocity dispersion than the surrounding gas.

From the temperature and velocity dispersion, one can estimate the non-thermal turbulence scale using

$$\sigma_{\rm nt} = \sqrt{\sigma_v^2 - \frac{k_{\rm B} T_{\rm kin}}{m_{\rm mol}}}, \quad (2)$$

where $m_{\rm mol}$ is the molecular mass, which is $m_{\rm mol} = m_{\rm N_2H^+} = 29 m_{\rm H}$. Adopting a kinetic temperature of $T_{\rm kin} = T_{\rm ex} = 15$ K, the observed σ_v range leads to $\sigma_{\rm nt} = 0.03$ to 0.24 km s^{-1}. Compared to the average sound speed of $c_s = \sqrt{k_{\rm B} T_{\rm kin}/\mu m_{\rm H}} = 0.23$ kms^{-1}, the filaments tend to have an overall subsonic but non-zero level of turbulence, i.e. $0 < \sigma_{\rm nt}/c_s \leq 1$. And the slightly decreased σ_v towards the centre would likely trace the turbulence decay during the dense core formation, which is comparable to the observed trend in infrared dark clouds (e.g. Wang et al. 2008).

4 ANALYSIS AND DISCUSSION

4.1 The column-density probability distribution function

As introduced in Section 1, the N-PDF, especially its high-density tail, could monitor the gas component with likely turbulence decay and increased self-gravity. To reveal the gas assembly around the intersections, we compared the N-PDF around the intersections and other areas on the filaments (denoted as filament paths). Around the intersections, the N-PDF is sampled in a circular area with $r = 7$ arcsec. Along the filament paths, it is sampled in a strip with width of $w = \overline{w}_{\rm fil,full} = 14''$. To make comparison, we also sampled the $N_{\rm tot}$ distribution in the observed region out of the ISF, which contains

Table 2. The physical properties of the gas structures.

Parameters	Cores	Filament paths[b]	Unit
$2R_{\rm maj}$[a]	8.5 ± 2.0, 3.3 ± 0.7	–	arcsec, 10^3 AU
$2R_{\rm min}$[a]	7.5 ± 2.0, 2.9 ± 0.3	–	arcsec, 10^3 AU
Length	–	5–60, 1.9–23	arcsec, 10^3 AU
Width	–	14 ± 4, 5.0 ± 1.5	arcsec, 10^3 AU
Mass	1.7 ± 0.5	2.0 ± 0.5	$M_\odot$
$\sigma_{\rm v}$[c]	0.12 ± 0.05	0.15 ± 0.07	km s^{-1}
$T_{\rm ex}$[d]	15 ± 3	15 ± 4	K
$N_{\rm tot}$[e]	4.0 ± 2.5	2.0 ± 0.5	10^{23} cm^{-2}

Notes. [a]The average FWHM diameter deconvolved with the synthesized beam size of 3 arcsec × 3 arcsec.
[b]For the filaments, the values represent the distribution of the filament paths. Each individual path represents a segment between two endpoints, and an endpoint could be either an intersection or a terminal.
[c]The velocity dispersion inferred from the observed line width as $\sigma_{\rm v} = \Delta V/\sqrt{8\ln 2}$.
[d]The N_2H^+ excitation temperature estimated from the spectral fitting.
[e]Derived from the integrated N_2H^+ emission using equation (1) and assuming N_2H^+ abundance of $X(N_2H^+) = 7.5 \times 10^{-10}$.

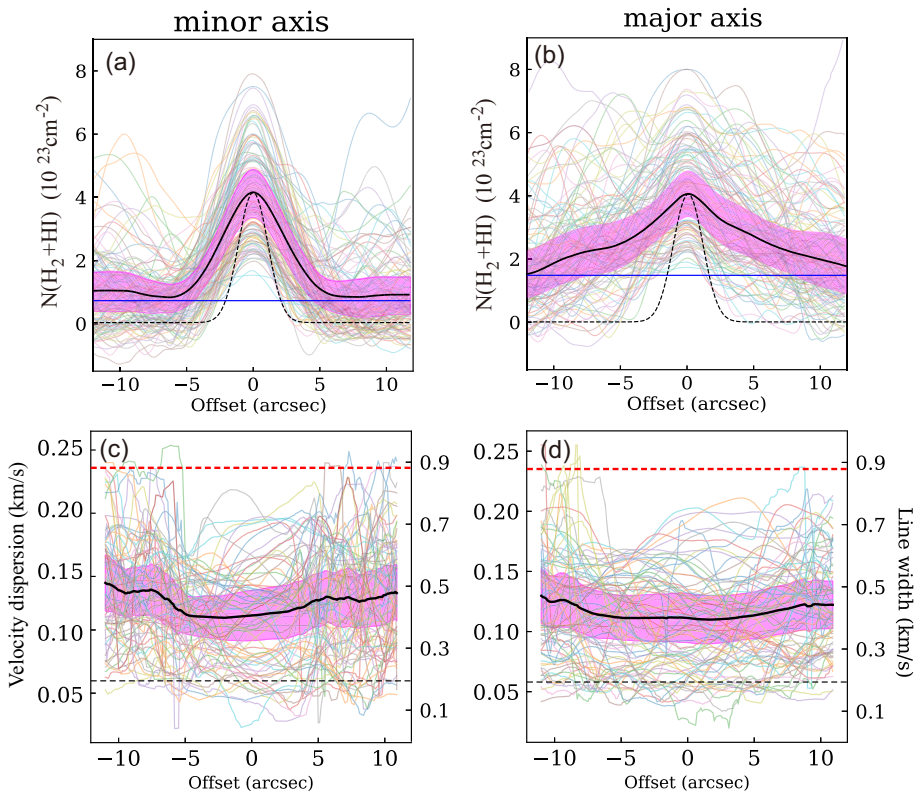

Figure 6. Upper panels: The column density profiles $N_{\rm tot}(r)$ over the dense cores (local emission peaks). Each profile is centred at the local emission peak. The thick solid black line represents the average profile for all the peaks. The light purple strip represents the standard deviation around the average level. The horizontal solid line indicates the average surrounding level of $N_{\rm tot}$ away from the cores. The dashed line represents the synthesized beam shape. The left-hand and right-hand panels are sampled along the minor and major axes of each peak, respectively. Lower panels: The velocity dispersion (line width) profiles of the N_2H^+ ($1_0 - 0_1$) line over the cores. In each panel, the solid line and strip also represent the average level and standard deviation, respectively. The red and black dashed lines represent the thermal motion at $T_{\rm kin} = 15$ K for the H_2 and N_2H^+ molecules, respectively.

the isolated gas patches and diffuse gas. Their $N_{\rm tot}$ distributions are shown in Fig. 7.

As shown in Fig. 7(a), the two components and outer region all have nearly Gaussian-shaped $N_{\rm tot}$ distributions. The outer region is peaked at nearly zero level and declines to half maximum at $N_{\rm tot} = 0.4 \times 10^{23}$ cm^{-2}, slightly higher than the 5σ detection limit. This is consistent with its major component of weak diffuse gas around or below the detection limit. The second component (filament paths) is peaked at $N_{\rm tot} = 0.4 \times 10^{23}$ cm^{-2} and is clearly separated from the component of outer region. The third component (intersections) is distributed towards further higher values, peaked at $N_{\rm tot} = 1.4 \times 10^{23}$ cm^{-2}. From their $N_{\rm tot}$ distributions, we can see that the diffuse gas components would not significantly affect the $N_{\rm tot}$-statistics of the filament paths and intersections.

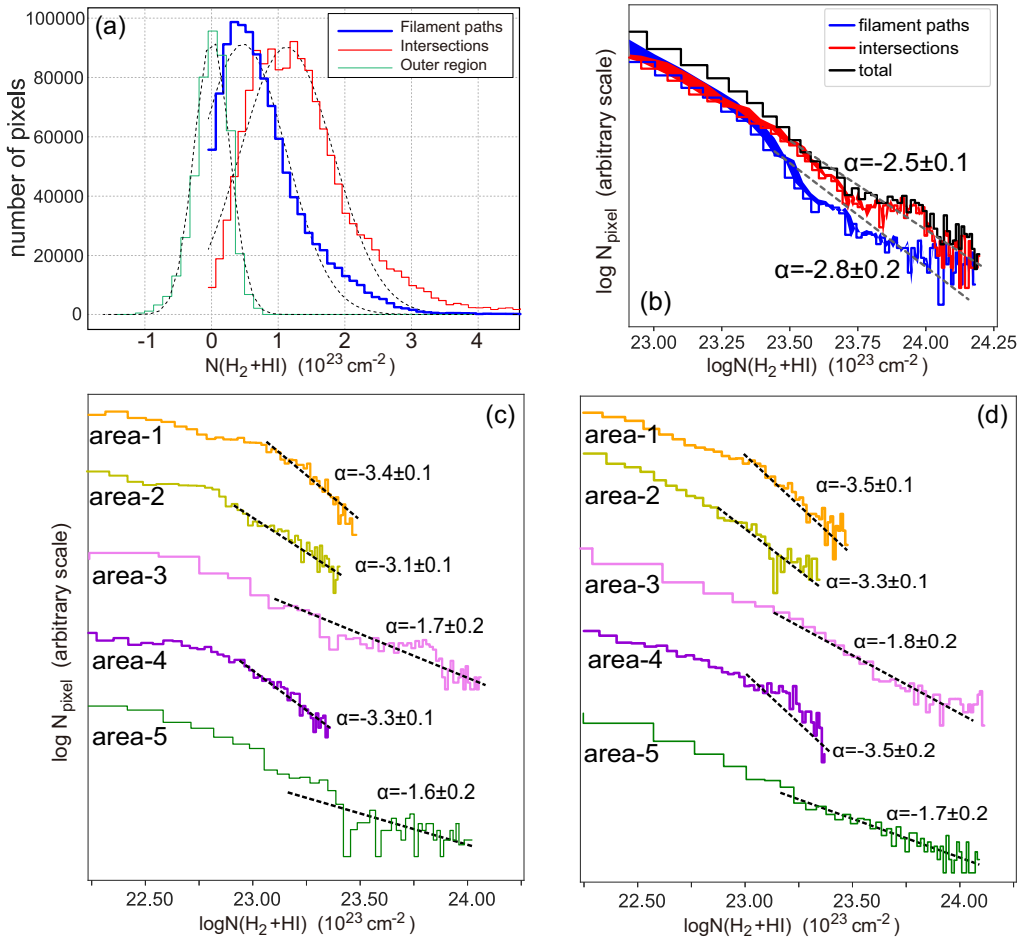

Figure 7. (a) The $N_{\rm tot}$ distributions of the three components in linear scale: intersections (red), filament paths (blue), and the outer region away from the ISF (green). The black dashed lines represent the Gaussian fitting for each component. (b) the $N_{\rm tot}$ probability distribution function (N-PDF) of the intersections (red line) and filaments (blue line) in logarithmic scale. The black line is the summation of the two components, namely the total N-PDF of the ISF. (c) and (d) The N-PDFs sampled in the sub-areas for (c) intersections and (d) the filament paths with the intersections excluded.

The $N_{\rm tot}$ distributions in the logarithmic scale, which are normally adopted to sample N-PDF, are presented in Fig. 7(b). The N-PDF would usually contain a lognormal component in lower $N_{\rm tot}$ range and a power-law tail towards the higher values (Kainulainen et al. 2009), with the second one possibly tracing the gas assembled due to the self-gravity. The transition from lognormal to power-law components occurs around $\log(N_{\rm tot}/{\rm cm}^{-2}) = 23.3$ to 23.5, corresponding to $N_{\rm tot} = (2.0 - 3.2) \times 10^{23}\,{\rm cm}^{-2}$. At $\log N_{\rm tot} > 23.3$, the N-PDF profiles of the both components switch into steeper slopes that can be fitted by a power-law shape of $dN_{\rm count}/d(\log N_{\rm tot}) \propto N_{\rm tot}^{\alpha}$. The best-fitting indices are $\alpha = -2.8 \pm 0.2$ and -2.5 ± 0.1 for the filaments and intersections, respectively.

Compared to the intersections, the filament paths have more drastic decline over the transition point, their N-PDF drops to much lower level than the intersections when $\log N_{\rm tot} > 23.3$. Towards higher $N_{\rm tot}$ values, the intersections have a pixel counting higher than the filaments by a factor of 4. The intersections have not only higher $N_{\rm tot}$ but also a bump-like feature above the average power-law trend in the range of $\log N_{\rm tot} = 23.7$ to 24.0. This range is comparable to the peak values in the $N_{\rm tot}(r)$ profiles (Fig. 6, upper panels), suggesting that the dense cores should have a major contribution to the $N_{\rm tot}$ bump.

4.2 Inspecting the spatial variation of the N-PDF

In addition to the global N-PDF, we also sampled the N-PDF over the different areas to inspect whether its variation has a real connection to the intersections or is merely due to the random fluctuation.

First, we calculated the N-PDF in each sub-area, as shown in Figs 7(c) and (d), wherein intersections and filament paths are also separately measured. As a result, among all the sub-areas, the intersections have higher α values than the filament paths, suggesting that the more flattened N-PDF tails around the intersections should be a common trend.

As shown in Figs 7(c) and (d), Area-3 and 5 have not only higher α than the other three sub-areas, but also highest $N_{\rm tot}$ that extend to $10^{24}\,{\rm cm}^{-2}$. One can see that Area-3 contains the most massive clump OMC-2 FIR-4 in Orion A north, which has a total mass of 39 to 80 $M_{\odot}$ as measured with different tracers and instruments (Nutter & Ward-Thompson 2007; Crimier et al. 2009; Sadavoy et al. 2010; López-Sepulcre et al. 2013). Area-5 also has a clump with considerable mass of 3–4 $M_{\odot}$ (Nutter & Ward-Thompson 2007; Sadavoy et al. 2010). Although the other sub-areas also have relatively high total masses ($\geq 6\,M_{\odot}$), their overall gas distributions appear more extended and do not contain such dense and compact parental clumps over the filament structures. The comparison suggests that α

would increase in the gas structures located in compact and massive clumps.

As a more detailed inspection, we estimated the N-PDF distribution over all the filament paths. We sampled the N-PDF along the filament paths in a step of 1.3 arcsec (nearly half beam size). At each point, the N-PDF is measured in a circular area with radius of 14 arcsec. A number of selected N-PDF profiles over OMC-2,3 region are presented in Fig. 8(a). These N-PDF profiles all evidently exhibit a turn-over to the power-law tail at the column density range of $\log N_{\rm tot} > 23.2$.

Figs 8(b) and (c) show the $\overline{N}_{\rm tot}$ and α distributions over the filaments in OMC-3, respectively. We note that the N-PDF distribution over entire OMC-2,3 region will be presented in subsequent works. As Fig. 8 shows, $\overline{N}_{\rm tot}$ and α distributions exhibit comparable variation trends. In particular, the area of MMS-2,3 has the highest values in both $\overline{N}_{\rm tot}$ and α.

For each point on the filament paths with N-PDF sampling, we measured its distance from the nearby intersection, denoted as d_i. The $\overline{N}_{\rm tot}$ and α distributions as functions of d_i are shown in Figs 9(a) and (b), respectively. The two parameters both have much higher values around $d_i = 0$ and a rapid decline towards larger d_i. In Fig. 9(a), the gas component with $\overline{N}_{\rm tot} > 2.0 \times 10^{23}$ cm^{-2} is confined within $d_i \leq 12$ arcsec and become largely absent beyond this limit. The average level (black squares with error bars) exhibits a smooth decline with d_i. In Fig. 9(b), α decreases from $\alpha = -2.4$ to -3.3 over $d_i = 0$ to 15 arcsec, and then rises again towards $d_i =$ 25 arcsec. The rising feature at the high end could be due to the several individual dense cores away from the intersections. Based on these decreasing trends with d_i, the intersections should have a significant trend of assembling dense gas. From Fig. 9, one can also see that the gas component with high-$N_{\rm tot}$ also tends to have higher α. According to the theoretical N-PDF analysis (Krumholz et al. 2005; Hennebelle & Chabrier 2011; Padoan & Nordlund 2011), it suggests that the gas therein could be more intensely bounded by the self-gravity.

However, as shown in Fig. 9(a), around the intersections there are also a large amount of gas with relatively low column density, i.e. $\overline{N}_{\rm tot} < 2.0 \times 10^{23}$ cm^{-2}. This amount of gas has low power-law slope of $\alpha = -6.5$ to -2.0 as shown in Fig. 9(b). It suggests that some intersections do not have largely increased $N_{\rm tot}$. In other words, the intersected filaments should be a necessary but not sufficient condition for assembling the dense cores.

4.3 The gravitational instabilities

Due to their low turbulence (Fig. 6), the candidate cores should be possibly bounded by the self-gravity. We calculated their virial masses, which can monitor the binding state due to the self-gravity. For an ellipsoidal core, the virial mass can be calculated following Li et al. (2013):

$$M_{\rm vir} = \frac{5}{\alpha\beta}\frac{\bar{r}\,c_{\rm s,eff}^2}{G}, \tag{3}$$

where $\bar{r}$ is the average core radius, $\alpha = (1 - a/3)/(1 - 2a/5)$ is a correction factor for the power-law density profile of $\rho \propto r^{-a}$. Using the value of $a = 1.6$ for an isothermal cloud in equilibrium, we would have $\alpha = 1.3$. $\beta = \arcsin e/e$ is the geometry factor to account for the eccentricity $e = \sqrt{1 - f^2}$, where f is the intrinsic ratio between minor and major axes. It can be estimated from the observed value using $f = (2/\pi) f_{\rm obs} F_1(0.5, 0.5, -0.5, 1.5, 1, 1 - f_{\rm obs}^2)$, where F_1 is the first-kind Appell hypergeometric function, and $f_{\rm obs} = (r_{\rm min}/r_{\rm maj})_{\rm obs}$. Based on equation (2), the effective sound speed $c_{\rm s,\,eff}$ can be estimated using

$$\begin{aligned} c_{\rm s,eff} &= \sqrt{c_{\rm s}^2 + \sigma_{\rm nt}^2} \\ &= \sqrt{\sigma_{\rm obs}^2 + k_{\rm B}T_{\rm kin}\left(\frac{1}{\mu m_{\rm H}} - \frac{1}{m_{\rm mol}}\right)}. \end{aligned} \tag{4}$$

If the core mass satisfies $M_{\rm core} \geq M_{\rm vir}$, i.e. $\alpha_{\rm vir} = M_{\rm vir}/M_{\rm core} \leq 1.0$, the thermal-and-kinetic energy should be lower than the potential well of the self-gravity so that the core would tend to be constrained by the self-gravity.

Another criterion to evaluate the core stability is the Bonner–Ebert (BE) mass, which would more specifically represent the mass upper-limit for a stable core because it considers two additional physical conditions, density gradient throughout the core and the external pressure. These two factors are important for constraining the gas in a dense core. The BE mass is estimated following the classical method (Stahler & Palla 2005) as:

$$M_{\rm BE} = \frac{m_1 c_{\rm s,eff}^4}{P_{\rm ic}^{\frac{1}{2}} G^{\frac{3}{2}}} \tag{5}$$

wherein $m_1 = 1.18$, $P_{\rm ic} = n_{\rm ic}\mu m_{\rm H}\sigma_{\rm ic}$ is the external pressure on to the dense core, which depends on the external gas number density $n_{\rm ic}$ and velocity dispersion $\sigma_{\rm ic}$. The NH_3 (1,1) and (2,2) observation with the Green Bank Telescope (GBT) (Kirk et al. 2017) reveals an average pressure of $P_c/k_{\rm B} = 2 \times 10^7$ K cm^{-3} in the Orion A dense cores with a small variation. The single-dish NH_3 cores sampled at a resolution of 10 arcsec should be comparable to the spatial sizes of the parental gas clumps of the filaments observed in this work. It should be thus reasonable to adopt an approximation of $P_{\rm ic} = P_c$ in our calculation.

Following Li et al. (2013), we also estimated the mass fraction that can be supported by the magnetic field B,

$$M_\Phi = c_\Phi \frac{\pi B \bar{r}^2}{G^{1/2}}, \tag{6}$$

wherein the coefficient is $c_\Phi = 0.12$, and the magnetic field in OMC-2,3 could vary from $B = 0.64$ to 0.85 mG (Houde et al. 2004; Matthews et al. 2005), causing a mass range of $\overline{M}_\Phi = 0.14$ to $0.19\,M_\odot$ at the average radius of $\bar{r} = 5.3 \times 10^{-3}$ pc. Combining the hydrostatic and magnetic components together, we have the critical mass of

$$M_{\rm crit} = M_{\rm BE} + M_\Phi, \tag{7}$$

The physical properties of the N_2H^+ cores and the derived $M_{\rm crit}$ and $M_{\rm vir}$ are presented in four diagrams in Fig. 10.

Fig. 10(a) shows the $c_{\rm s,\,eff}$ and $M_{\rm core}$ distributions. The N_2H^+ cores have $c_{\rm s,\,eff} = 0.25$ to 0.5 km s^{-1} and $M_{\rm core} = 0.07$ to $1.8\,M_\odot$. The major fraction of the cores have $c_{\rm s,\,eff} < 0.35$ kms^{-1}. Although several cores with high masses tend to have slightly increased $c_{\rm s,\,eff}$, the overall sample does not have noticeable correlation between $c_{\rm s,\,eff}$ and $M_{\rm core}$. It suggests that low turbulence should be a universal state for all the cores in spite of their masses.

Fig. 10(a) also shows the 850 μm cores observed with JCMT/SCUBA-2 (Kirk et al. 2017), wherein the cores associated with the N_2H^+ filaments are denoted with the black-edged diamonds. The velocity dispersion of the 850 μm cores were measured from the GBT NH_3 lines. The major fraction of these cores have $M_{\rm core} =$ 0.18 to $3.0\,M_\odot$, while the parental cores of the N_2H^+ filaments (black-edged diamonds) tend to have relatively high masses from 0.7 to $10\,M_\odot$. It suggests the relatively high-mass cores are located within the ISF. The three samples of cores also have distinct $c_{\rm s,\,eff}$

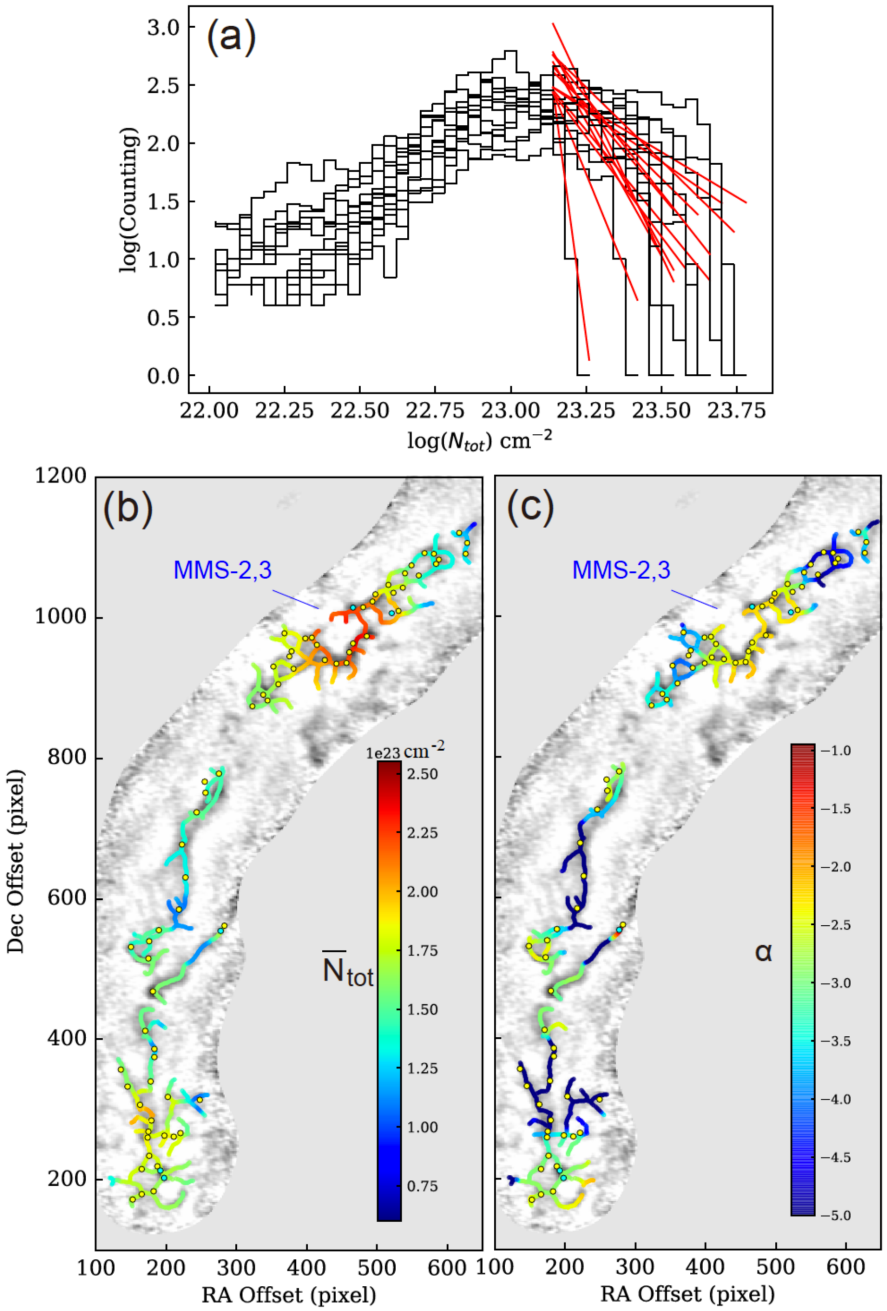

Figure 8. (a) A number of N-PDF profiles overlaid to show the N-PDF variation. The red lines represent the power-law fitting to each N-PDF in the range of $\log N_{\rm tot} > 23.2\,{\rm cm}^{-2}$. At each point, the N-PDF is measured in a circular area with $r = 14$ arcsec. (b) The average $N_{\rm tot}$ distribution over the filament paths in OMC-3. (c) The distribution of N-PDF power-law tail index α over the filament paths in OMC-3. The $\overline{N}_{\rm tot}$ and α distributions are measured over the filament paths with a spatial interval of 1.3 arcsec (nearly half beam size) in order to keep a uniform Nyquist spatial sampling.

distributions. The parental cores have lower average $c_{\rm s,\,eff}$ than the other 850 μm cores. And the N_2H^+ cores have further lower $c_{\rm s,\,eff}$ than their parental cores. This comparison suggests a decline trend for the turbulence from large to small scales, in particular towards the inner regions of the large-scale cores.

Fig. 10(b) shows the $M_{\rm core}$ and $r_{\rm core}$ distribution of the N_2H^+ cores. It shows that $M_{\rm core}$ is increasing with $r_{\rm core}$. Their relation can be best fit with a power law of

$$\frac{M_{\rm core}}{M_\odot} = 5.8 \times 10^{-3} \left(\frac{r}{10^{-3}\,{\rm pc}} \right)^{2.9}. \quad (8)$$

The power-law index (2.9) is close to 3.0, suggesting that the cores have similar number densities, so that the core mass can be approximated as $M_{\rm core} = \mu m_{\rm H} n_{\rm core} (4/3)\pi r^3$. The average number density is estimated to be $n = (1.8 \pm 0.6) \times 10^7\,{\rm cm}^{-3}$. The 850 μm cores have $r > 0.017$ pc and their radii are not overlapped with the N_2H^+ cores (insert panel). This is due to the lower limit of $r_{\rm core}$ set by the JCMT beam size. From their $M(r)$ distribution, the 850 μm cores are estimated to have much lower densities of $n = (2.0 \pm 1.5) \times 10^6\,{\rm cm}^{-3}$. In comparison, the average density of the N_2H^+ cores ($1.8 \times 10^7\,{\rm cm}^{-3}$) would represent a characteristic value of the dense-gas assembly in the large-scale

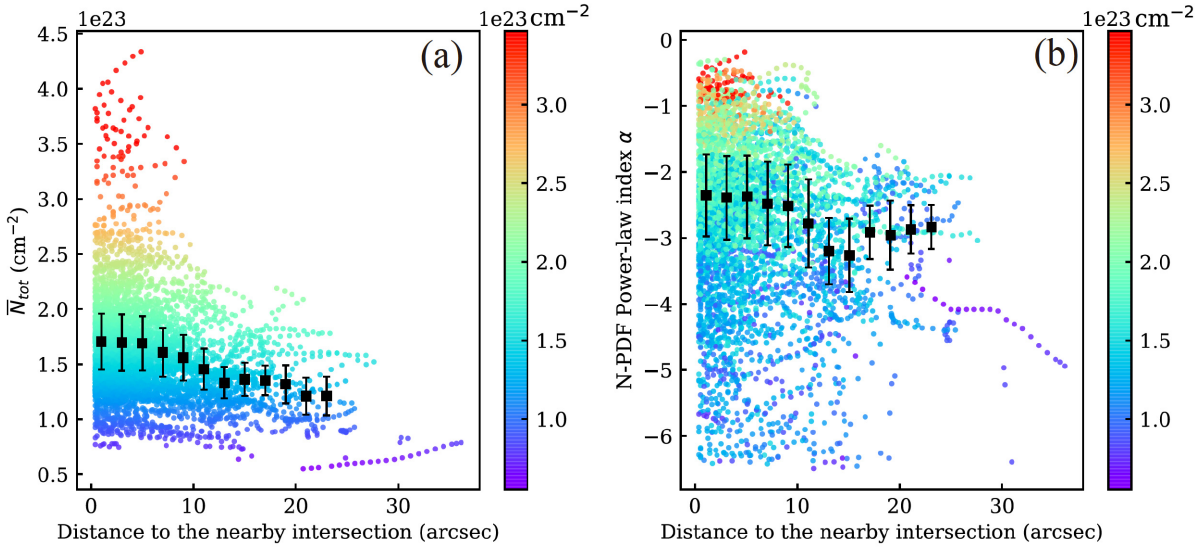

Figure 9. The distribution of the parameters with the distance from each sampled position to its nearest intersection, d_i, for the positions over the filament paths in OMC-2,3 (see Figs 8b and c for OMC-3). The squares with the error bars represent the average value and standard deviation within each interval, which has a width of $\Delta d_i = 2$ arcsec. (a) The distribution of $\overline{N}_{\rm tot}$ with d_i. (b) The distribution of α with d_i. In both (a) and (b), the colour scale represents $\overline{N}_{\rm tot}$.

cores. As suggested by the difference in $c_{\rm s,\,eff}$ between the 850 μm and N_2H^+ cores, the gas assembly would be closely related to the turbulence dissipation. During the turbulence dissipation, the dense gas would gradually reach a hydrostatistic equilibrium (BE sphere). In this condition, the cores would have a limited possibility for further compression, unless they collapse into protostars.

In Fig. 10(b), the theoretical functions of $M_{\rm vir}(r)$ and $M_{\rm crit}(r)$ are also plotted. They are calculated from equations (3) and (7), respectively. In calculation, an average value of $c_{\rm s,\,eff} = 0.3\,{\rm km\,s^{-1}}$ is adopted. As shown in the diagram, the cores mostly have $M_{\rm core} > M_{\rm vir}$ (super-virial), with only about ten cores having $M_{\rm core} < M_{\rm vir}$ (sub-virial). In comparison, a much more fraction of the cores have $M_{\rm core} < M_{\rm crit}$ (sub-critical). It is noteworthy that $M_{\rm crit}(r)$ has a minor but not negligible contribution from $M_\Phi(r)$, namely the magnetic field. Because of the M_Φ-contribution, $M_{\rm crit}(r)$ rises above the $M_{\rm BE}$ level for a scale of $\sim 0.3\,M_\odot$ towards large radius. As a result, about $\sim$10 cores are located between the two levels, namely $M_{\rm BE} < M_{\rm core} < M_{\rm crit}$. For these cores, the magnetic field may play a significant support against the self-gravity.

To more specifically estimate the stability of the individual cores, we derived the virial parameter $\alpha_{\rm vir} = M_{\rm vir}/M_{\rm core}$ and critical mass ratio $\alpha_{\rm crit} = M_{\rm crit}/M_{\rm core}$. The $\alpha_{\rm vir}(M_{\rm core})$ and $\alpha_{\rm crit}(M_{\rm core})$ distributions are shown in Figs 10(c) and (d), respectively. Actually, these two diagrams exhibit similar results with Fig. 10(b) except a slight difference in the number of cores above and below each threshold. As shown in the two panels, most cores (7 exceptions) have $\alpha_{\rm vir} < 1$, suggesting them to be bounded by the self-gravity. A less fraction of the cores, about 30 (23 per cent), have $\alpha_{\rm crit} < 1$. This result indicates that cores are confined by the self-gravity, but only about one fifth of the cores would have the tendency to collapse into protostars.

It is noted that there are two uncertainties in deriving the core instabilities. First, it is uncertain whether the magnetic support is comparable to that characterized by M_Φ and whether most cores have similar B-field with the previous measurement. As shown in Fig. 10(b), if only using $M_{\rm BE}$, the super critical cores would moderately increase by a number of $\sim$10, or a fraction increased to 30 per cent.

Secondly, the external pressure $P_{\rm ic}$ is also from a less direct estimation. The actual value may be lower ($P_{\rm ic} < P_{\rm c}$), because the single-dish cores (Kirk et al. 2017) may not thoroughly and uniformly harbour the N_2H^+ filaments. Moreover, in a clump, the pressure would decline from its centre to outside, so the confinement to the internal filaments by the thermal pressure could be less effective. To increase the instabilities, one may consider other factors such as the dynamical pressure due to the external gas motions. For example, the gas converging flows along the filaments with several km s^{-1} would compress the central region, providing a dynamical pressure comparable to $P_{\rm ic}$. Since the gas flows are frequently observed in Orion and other regions from large to small scales (e.g. Peretto et al. 2014; Hacar, Tafalla & Alves 2017; Yuan, Li & Wu 2018; Chen et al. 2019b), they may considerably affect the core instability. However, the external perturbation would also inject hot gas and kinetic energy into the cores, increasing the temperature and turbulence, letting them become even less bound. Considering that $M_{\rm BE}$ is much more sensitive to $c_{\rm s,\,eff}$ than $P_{\rm ic}$ (equation 5), the external perturbation is more likely to have a negative effect to the binding state of the cores unless the input energy can be efficiently dissipated. Based on all these factors, at the current state, the cold dense cores in Orion A seem unlikely to have very extensive star-forming activities.

4.4 The efficiency of star formation

From the integrated N_2H^+ emission and using equation (1), we estimated a total gas mass of 350 $M_\odot$ for the ISF in OMC-2,3 region. In comparison, the dense cores altogether have a total mass of 69 $M_\odot$, taking up 20 per cent of the total gas mass. We thus suggests a core-formation efficiency (CFE) of $\sim$0.2 for the cold dense gas ($T \simeq 15$ K, $n > 10^5$ cm^{-3}) in Orion A north.

From the dust continuum observation in Orion B, Könyves et al. (2020) measured a CFE of 0.01 to 0.2 from the Herschel 70 to 500 μm images at a typical resolution of 18 arcsec. In particular, the relatively

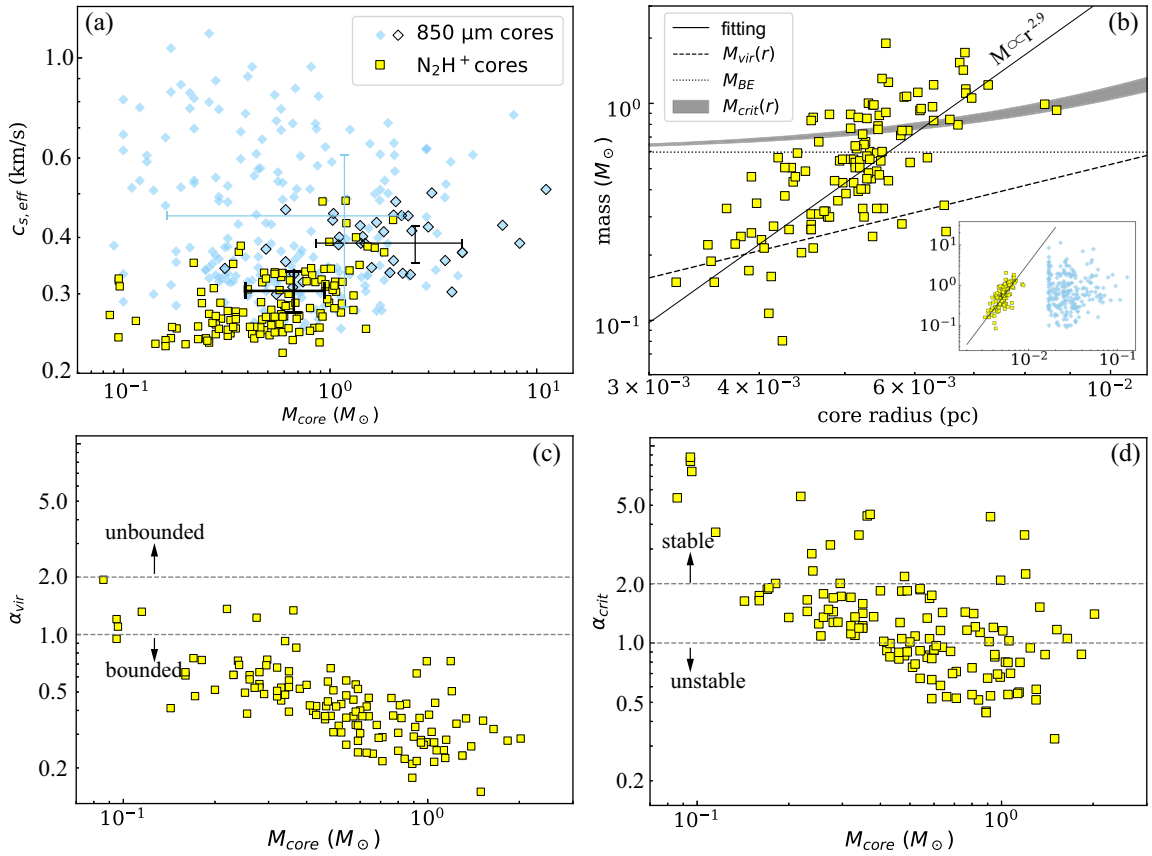

Figure 10. The distributions of the core parameters. (a) The diagram of effective sound speed $c_{s,\,eff}$ and the core mass M_{core} for the N_2H^+ cores. The yellow squares represent the N_2H^+ cores in this work, while the diamonds represent the 850 μm dusty cores (Kirk et al. 2017) whose $c_{s,\,eff}$ values are calculated from σ_{obs} and T_{kin} values (Table 1) using equation (4). The 850 μm cores are sampled over a spatial scale of 12 pc, with Orion BN/KL and Orion A South regions also included. In Kirk et al. (2017) a spatially coherent GBT NH_3 observation was also performed to measure σ_{obs} and T_{kin} of the cores. Among the 850 μm cores, the black-edged diamonds represent those overlapped with the N_2H^+ emission, thus the possible parental cores of the N_2H^+ filaments and cores. The solid error bars represent the average values and standard deviation of the three samples, N_2H^+ cores (thick black lines), the 850 μm cores associated with the N_2H^+ emission (thin black lines), and the entire sample of the 850 μm cores (blue lines). (b) The distribution of the core mass and radius. The core radius represents the average value of the major and minor axes. The solid line represents the power-law fitting to the data points. The virial mass and BE mass are plotted in dashed and dotted lines, respectively. The grey strip represents the $M_{crit}(r)$ range due to the magnetic field variation between 0.64 and 0.85 mG (Houde et al. 2004; Matthews et al. 2005). The insert panel shows the data 850 μm dusty cores in blue diamonds. In calculation of $M_{vir}(r)$ and $M_{crit}(r)$, an average value of $c_{s,\,eff} = 0.3\,km\,s^{-1}$ is assumed. (c) The diagram of M_{core} and M_{vir}. The dashed lines represent the levels of $\alpha_{vir} = 1$ and 2. (d) The distribution of M_{core} and M_{crit}. The dashed lines also represent $\alpha_{crit} = 1$ and 2, respectively. In (c) and (d), M_{vir} and M_{crit} are calculated from the $c_{s,\,eff}$ values of the individual cores instead of using the average values.

high column-density regions ($A_V > 7$ or $N_{tot} > 10^{22}\,cm^{-2}$) exhibit a relatively high value of CFE>0.1, which is comparable to the value in OMC-2,3. The similarity of CFEs at large and small scales could be maintained by the self-similar structures in filamentary clouds. In this study, the N_2H^+ filaments could more particularly trace the dense gas that has low turbulence and are more confined by self-gravity. It therefore exhibits higher CFE than the single-dish cores observed at larger scales, which contain more extended and turbulent gas.

Compared to the CFE, the fraction of gas mass to eventually form stars is more uncertain. Currently there is no confirmed protostellar objects among our N_2H^+ cores since the cores are all displaced from the catalogued YSOs (Megeath et al. 2012). Among the cores, we would first consider the supercritical ones ($M > M_{crit}$) as the star-forming candidates, which have a total mass of $\sim 50\,M_\odot$. Assuming a stellar-to-core mass ratio of $\epsilon = 0.8$ (Beuther et al. 2002; Wang et al. 2010), we can estimate an upper limit of total stellar mass to be $40\,M_\odot$.

5 SUMMARY AND CONCLUSION

We investigated the cold dense filaments and cores in OMC-2,3 region in Orion A North using the ALMA N_2H^+ (1-0) line emission, in particular the isolated hyperfine component $JF_1 = 1_0$-0_1. The filament paths were extracted using the DisPerSE algorithm. From the comparative study between dense gas distribution and the filament structure, we explored the physical properties in four major aspects.

(1) The filament extraction reveals the spatial and velocity distributions of the intersected filaments. With the likely pseudo-ones excluded, there are more than 170 intersections for the filaments in the ISF over a spatial scale of 2 pc. They have single-velocity component with relatively narrow line width ($\Delta V \leq 0.6\,km\,s^{-1}$), thus would represent the different filaments being merged together instead of merely overlapped in projection.

(2) Along the main body of integral-shaped filament (ISF), 128 candidate cores are identified from the local emission peaks above the 5 σ detection limit. The cores have small velocity dispersion of σ = 0.03 to 0.24 km s^{-1} and a mass distribution from 0.07 to 1.9 $M_{\odot}$. A large fraction of the cores (103) are located around the intersections with offset less than 5 arcsec, while only a small fractions (25) are located on the long filament paths or displaced from the ISF. The comparison shows that the intersections would play a significant role in assembling the local dense gas, while the fragmentation of individual filament path into the cores are less prominent in our observed spatial scale (0.005 to 0.01 pc).

(3) The N-PDFs of the intersections and other part of filaments both have an evident power-law tail towards high column densities, i.e. $\log(N_{\rm tot}/{\rm cm}^{-2}) > 23.3$. But the areas with high $N_{\rm tot}$ are mainly associated the intersections, and the power-law index of the N-PDF tail also exhibits an increasing trend towards the intersections, in agreement with the dense gas assembly therein.

(4) Most of the cores (7 exceptions) have virial parameter of $\alpha_{\rm vir} \leq 1$. They should represent a sample of cold dense prestellar cores in OMC-2,3. However, only 23 per cent of the cores may have potential to collapse into protostars due to their low critical mass ratio ($\alpha_{\rm crit} \leq 1$), while the other cores could be more stabilized by the internal velocity dispersion and magnetic field. In general, the cold prestellar cores in OMC-2,3 may require further mass growth or other perturbations to more broadly initiate their star formation.

ACKNOWLEDGEMENTS

We thank the referee for very detailed comments that help improve the scientific analysis. This work is supported by the National Natural Science Foundation of China No. 11988101, No. 11725313, No. 11403041, No. 11373038, No. 11373045, No. U1931117, CAS International Partnership Program No. 114A11KYSB20160008, and the Young Researcher Grant of National Astronomical Observatories, Chinese Academy of Sciences. This paper makes use of the following ALMA data: ADS/JAO.ALMA#2013.1.00662.S. ALMA is a partnership of ESO (representing its member states), NSF (USA) and NINS (Japan), together with NRC (Canada), MOST and ASIAA (Taiwan region), and KASI (Republic of Korea), in cooperation with the Republic of Chile. The Joint ALMA Observatory is operated by ESO, AUI/NRAO and NAOJ.

DATA AVAILABILITY

The data underlying this article will be shared on reasonable request to the corresponding author.

REFERENCES

André P. et al., 2010, A&A, 518, L102
Arzoumanian D. et al., 2011, A&A, 529, L6
Bergin E. A., Langer W. D., 1997, ApJ, 486, 316
Beuther H., Schilke P., Sridharan T. K., Menten K. M., Walmsley C. M., Wyrowski F., 2002, A&A, 383, 892
Caselli P., Walmsley C. M., Zucconi A., Tafalla M., Dore L., Myers P. C., 2002, ApJ, 565, 344
Chen C.-Y. et al., 2019a, MNRAS, 490, 527
Chen H.-R. V. et al., 2019b, ApJ, 875, 24
Chen H. H.-H., Burkhart B., Goodman A., Collins D. C., 2018, ApJ, 859, 162
Chira R.-A., Beuther H., Linz H., Schuller F., Walmsley C. M., Menten K. M., Bronfman L., 2013, A&A, 552
Clarke S. D., Whitworth A. P., Hubber D. A., 2016, MNRAS, 458, 319
Crimier N., Ceccarelli C., Lefloch B., Faure A., 2009, A&A, 506, 1229
Da Rio N. et al., 2016, ApJ, 818, 59
Federrath C., Klessen R. S., 2013, ApJ, 763, 51
Ginsburg A., Mirocha J., 2011, PySpecKit: Python Spectroscopic Toolkit, record ascl:1109.001
Gómez G. C., Vázquez-Semadeni E., Zamora-Avilés M., 2018, MNRAS, 480, 2939
Hacar A., Tafalla M., Kauffmann J., Kovács A., 2013, A&A, 554, A55
Hacar A., Tafalla M., Alves J., 2017, A&A, 606, A123
Hacar A., Tafalla M., Forbrich J., Alves J., Meingast S., Grossschedl J., Teixeira P. S., 2018, A&A, 610, A77
Hennebelle P., Chabrier G., 2011, ApJ, 743, L29
Hennemann M. et al., 2012, A&A, 543, L3
Henshaw J. D., Caselli P., Fontani F., Jiménez-Serra I., Tan J. C., 2014, MNRAS, 440, 2860
Henshaw J. D. et al., 2016, MNRAS, 463, 146
Hill T. et al., 2011, A&A, 533, A94
Houde M., Dowell C. D., Hildebrand R. H., Dotson J. L., Vaillancourt J. E., Phillips T. G., Peng R., Bastien P., 2004, ApJ, 604, 717
Johnstone D., Bally J., 1999, ApJ, 510, L49
Kainulainen J., Beuther H., Henning T., Plume R., 2009, A&A, 508, L35
Kainulainen J., Stutz A. M., Stanke T., Abreu-Vicente J., Beuther H., Henning T., Johnston K. G., Megeath S. T., 2017, A&A, 600, A141
Kirk H. et al., 2017, ApJ, 846, 144
Kirk H., Klassen M., Pudritz R., Pillsworth S., 2015, ApJ, 802, 75
Koch E. W., Rosolowsky E. W., 2016, FilFinder: Filamentary structure in molecular clouds, Astrophysics Source Code Library, record ascl:1608.009
Könyves V. et al., 2020, A&A, 635, A34
Kounkel M. et al., 2017, ApJ, 834, 142
Krumholz M. R., McKee C. F., Klein R. I., 2005, Nature, 438, 332
Li D., Kauffmann J., Zhang Q., Chen W., 2013, ApJ, 768, L5
Lin Y. et al., 2017, ApJ, 840, 22
Lin Y., Csengeri T., Wyrowski F., Urquhart J. S., Schuller F., Weiss A., Menten K. M., 2019, A&A, 631, A72
Liu T. et al., 2018, ApJ, 859, 151
López-Sepulcre A. et al., 2013, A&A, 556, A62
Matsushita Y., Takahashi S., Machida M. N., Tomisaka K., 2019, ApJ, 871, 221
Matthews B. C., Lai S.-P., Crutcher R. M., Wilson C. D., 2005, ApJ, 626, 959
Megeath S. T. et al., 2012, AJ, 144, 192
Miettinen O., 2014, A&A, 562, A3
Motte F., Bontemps S., Louvet F., 2018, ARA&A, 56, 41
Myers P. C., 1983, ApJ, 270, 105
Myers P. C., 2011, ApJ, 735, 82
Nutter D., Ward-Thompson D., 2007, MNRAS, 374, 1413
Padoan P., Nordlund Å., 2011, ApJ, 730, 40
Pagani L., Daniel F., Dubernet M. L., 2009, A&A, 494, 719
Peretto N. et al., 2014, A&A, 561, A83
Pon A., Johnstone D., Heitsch F., 2011, ApJ, 740, 88
Ragan S. et al., 2012, A&A, 547, A49
Ren Z., Li D., Chapman N., 2014, ApJ, 788, 172
Sadavoy S. I. et al., 2010, ApJ, 710, 1247
Salji C. J. et al., 2015, MNRAS, 449, 1769
Schneider N. et al., 2012, A&A, 540, L11
Schneider S., Elmegreen B. G., 1979, ApJS, 41, 87
Schöier F. L., van der Tak F. F. S., van Dishoeck E. F., Black J. H., 2005, A&A, 432, 369
Shimajiri Y. et al., 2015, ApJS, 217, 7
Shimajiri Y., André P., Ntormousi E., Men'shchikov A., Arzoumanian D., Palmeirim P., 2019, A&A, 632, A83
Shirley Y. L., 2015, PASP, 127, 299
Smith R. J., Glover S. C. O., Klessen R. S., Fuller G. A., 2016, MNRAS, 455, 3640
Sousbie T., 2011, MNRAS, 414, 350
Stahler S. W., Palla F., 2005, The Formation of Stars, Wiley-VCH, Weinheim
Starck J. L., Donoho D. L., Candès E. J., 2003, A&A, 398, 785
Takahashi S., Ho P. T. P., Teixeira P. S., Zapata L. A., Su Y.-N., 2013, ApJ, 763, 57

Tan J. C., Beltrán M. T., Caselli P., Fontani F., Fuente A., Krumholz M. R., McKee C. F., Stolte A., 2014, in Beuther H., Klessen R. S., Dullemond C. P., Henning T., eds, Protostars and Planets VI. University of Arizona Press, Tucson, AZ, p. 149
Treviño-Morales S. P. et al., 2019, A&A, 629, A81
Wang Y., Zhang Q., Pillai T., Wyrowski F., Wu Y., 2008, ApJ, 672, L33
Wang P., Li Z.-Y., Abel T., Nakamura F., 2010, ApJ, 709, 27
Wang J.-W. et al., 2019, ApJ, 876, 42
Xu J.-L., Xu Y., Zhang C.-P., Liu X.-L., Yu N., Ning C.-C., Ju B.-G., 2018, A&A, 609, A43
Yuan J., Li J. Z., Wu Y., 2018, in Tarchi A., Reid M. J., Castangia P., eds, Proc. IAU Symp. 336, Astrophysical Masers: Unlocking the Mysteries of the Universe. Cambridge University Press, Cambridge, p. 299

This paper has been typeset from a TEX/LATEX file prepared by the author.